Boron-assisted synthesis of compositionally complex amorphous oxides via short-range-order-constrained generative design

Honglin Li,[1,2] Chuhao Liu,[3,4,*] Yongfeng Guo,[2] Xiaoshan Luo,[1] Yijie Chen,[5] Guangsheng Liu,[6] Yu Li,[2] Ruoyu Wang,[7] Zhenyu Wang,[1] Jianzhuo Wu,[2] Shouwei Zuo,[8] Zhen Luo,[3] Cheng Peng,[3] Qinyu Jiang,[4] Jialu Li,[6] Cheng Ma,[1] Zhuohang Xie,[1] Jian Lv,[1] Yufei Ding,[9] Huabin Zhang,[8] Jian Luo,[2,6] Zhicheng Zhong,[7] Yuzhu Wang,[10] Mufan Li,[3,†] Yanchao Wang,[1,‡] and Wan-Lu Li[2,6,§]

[1]*Key Laboratory of Material Simulation Methods and Software of Ministry of Education,*
College of Physics, Jilin University, Changchun, China
[2]*Aiiso Yufeng Li Family Department of Chemical and Nano Engineering,*
University of California, San Diego, La Jolla, CA, USA
[3]*College of Chemistry and Molecular Engineering, Peking University, Beijing, China*
[4]*Institute of Molecular Engineering Plus, College of Chemistry, Fuzhou University, Fuzhou, China*
[5]*Institute of Modern Physics, Fudan University, Shanghai, China*
[6]*Program in Materials Science and Engineering, University of California, San Diego, La Jolla, CA, USA*
[7]*School of Artificial Intelligence and Data Science,*
University of Science and Technology of China, Hefei, China
[8]*Center for Renewable Energy and Storage Technologies, Physical Science and Engineering Division,*
King Abdullah University of Science and Technology, Thuwal, Kingdom of Saudi Arabia
[9]*Department of Computer Science and Engineering,*
University of California, San Diego, La Jolla, CA, USA
[10]*Shanghai Synchrotron Radiation Facility, Shanghai Advanced Research Institute, Shanghai, China*

These authors contribute equally to this work:
Honglin Li, Yongfeng Guo, Xiaoshan Luo, Yijie Chen

[*]*Corresponding Authors:*
Chuhao Liu - chuhao_liu@fzu.edu.cn
Mufan Li - mufanli@pku.edu.cn
Yanchao Wang - wyc@calypso.cn
Wan-Lu Li - wal019@ucsd.edu

(Dated: January 14, 2026)

Contents

S1. Supplementary Text S2
A. Algorithm for PDM Calculation S2
B. Evaluation of the generative model S4
C. Comparative Energy Evaluation of BCC, FCC, and HCP Structures S8
D. Hierarchical clustering dendrogram for the five lowest-energy structures. S9
E. Normalized variance of PDM S11
F. Validation of DPA-2 Energy Accuracy Against DFT Calculations S13
G. Diffusion rate analysis S14
H. Characterization S15
I. Catalytic performance of Group1-3 S21
J. Structural characterization of the twelve-component FeCoNiCuMnZnMoWAlSnBO$_x$ sample S22

---

[*] chuhao_liu@fzu.edu.cn
[†] mufanli@pku.edu.cn
[‡] wyc@calypso.cn
[§] wal019@ucsd.edu

S1 Supplementary Text

A. Algorithm for PDM Calculation

Below, we present the pseudocode for computing the PDM.

Algorithm 1 PDM calculation

```
Require: atomic positions $X \in \mathbb{R}^{N\times 3}$; atomic species (number) $\mathcal{S} = \{s_1, \dots, s_N\}$; lattice matrix $L \in \mathbb{R}^{3\times 3}$; cutoff $r_c = 5.0\,\text{Å}$
Ensure: unordered-pair map PDM$\{\alpha\beta \to n\}$
initialize $D \leftarrow \mathbf{0}^{N\times N}$                                  ▷ raw Euclidean distances
for $i \leftarrow 1$ to $N$ do
    for $j \leftarrow 1$ to $N$ and $i \neq j$ do
        $\delta \leftarrow X[j] - X[i] - \text{round}\big((X[j] - X[i])L^{-1}\big)L$      ▷ minimum-image shift
        $D[i,j] \leftarrow \|\delta\|$
    end for
end for
initialize PDM $\leftarrow \{(s_i, s_j) : 0 \mid s_i \le s_j,\ s_i, s_j \in \mathcal{S}\}$         ▷ empty dictionary
for $i \leftarrow 1$ to $N-1$ do
    for $j \leftarrow i+1$ to $N$ do
        if $D[i,j] < r_c$ then
            key $\leftarrow$ SORT($s_i$, $s_j$)                                     ▷ e.g., "AB"
            PDM[key] $\leftarrow$ PDM[key] $+ 1$
        end if
    end for
end for
```

Supplementary Algorithm 1 provides a direct computational recipe for the PDM defined in Equation 1. In a single pass it first builds the full pairwise distance matrix, using raw Euclidean norms and then applying the minimum-image convention under periodic boundary conditions so that each entry D_{ij} correctly reflects the shortest separation between atoms i and j. It then initializes an empty dictionary for PDM counts and loops over every unordered atom pair ($i < j$): whenever $D_{ij} < r_c$, the species labels (s_i, s_j) are sorted into a key (e.g. "AB") and that key's count is incremented by one. The final dictionary thus contains exactly the near-neighbour counts for all element pairs, which are assembled into the $K \times K$ PDM matrix used as the Cond-CDVAE conditioning descriptor.

To illustrate the construction of the Pair-Density Matrix (PDM), we consider a minimal four-atom *cubic* cell with lattice constant $a = 3.0$ Å.

Two A atoms are placed at $(0,0,0)$ and $(1,0,0)$, and two B atoms at $(0,1,0)$ and $(1,1,0)$ (Cartesian coordinates, units in ångströms throughout). Periodic boundary conditions (PBC) are applied; because all pairwise separations are smaller than $a/2$, no minimum-image wrapping occurs. For clarity we use a demonstration cut-off of $r_c^{\text{demo}} = 1.1$ Å (the production value elsewhere in the paper is 5.0 Å).

Exactly four unordered pairs—$(1,2)$, $(1,3)$, $(2,4)$, and $(3,4)$—lie within the cut-off. Applying the sorting-and-counting rule in Algorithm 1 gives

$$\text{PDM}_{AA} = 1, \qquad \text{PDM}_{AB} = 2, \qquad \text{PDM}_{BB} = 1,$$

so that, in the basis $\{A, B\}$,

$$\text{PDM}\big(r_c^{\text{demo}}\big) = \begin{pmatrix} 1 & 2 \\ 2 & 1 \end{pmatrix}.$$

The off-diagonal entry counts every distinct A–B neighbour pair, and the symmetry $\text{PDM}_{\alpha\beta} = \text{PDM}_{\beta\alpha}$ is enforced by construction. Running the same coordinates through our public script `compute_pdm.py` returns the same dictionary `{AA: 1, AB: 2, BB: 1}`, thereby validating Equation 1 and Algorithm 1.

TABLE S1: Inter-atomic distances in the 4-atom cell. An asterisk (*) marks pairs that satisfy $d_{ij} < r_c^{\text{demo}}$.

i	j	d_{ij} (Å)	species pair
1	2	1.000*	A–A
1	3	1.000*	A–B
1	4	1.414	A–B
2	3	1.414	A–B
2	4	1.000*	A–B
3	4	1.000*	B–B

B. Evaluation of the generative model

To evaluate the effectiveness of ApolloX in modeling complex disordered systems, we apply it to a representative multi-component composition, $Fe_{12}Co_{12}Ni_{12}Mo_{12}B_{12}O_{60}$ (120 atoms). To maintain charge neutrality while preserving an equimolar ratio among the metallic species and boron, we adopt a Fe:Co:Ni:Mo:B:O atomic ratio of 12:12:12:12:12:60. This chemically diverse, boron-rich oxide provides a stringent test bed for benchmarking ApolloX in predicting thermodynamic stability, short-range order, and structure–function relationships in amorphous or metastable materials.

A total of 10,000 candidate $Fe_{12}Co_{12}Ni_{12}Mo_{12}B_{12}O_{60}$ structures were generated by random elemental substitution on a BCC parent phase within a 120-atom cell. Analogous energy-distribution tests were also performed for FCC and HCP configurations, as discussed in Supplementary Section D. These structures form the initial dataset for training and evaluating the generative model.

The pair-density matrix (PDMs) of the structures were then used to train the conditional generative model (Cond-CDVAE). To assess the accuracy of this model, we selected a reference PDM as the target and generated 100 structures. As shown in Fig.S1A, the average pairwise differences between generated and target PDMs are below 25% for most element pairs.

We further evaluated reconstruction accuracy on a test set of 1,000 structures. For each target PDM, one structure was generated and the mean relative PDM error was computed by averaging over all matrix elements. As summarized in Fig.S1B, 90% of the generated structures exhibit mean relative errors below 20%, demonstrating that the generative model accurately captures the targeted CSRO characteristics. Novelty was assessed by comparing the 1,000 generated structures against the 80,000 structures in the training set. The novelty fraction, defined as the proportion of generated structures with no matches in the training data, decreases systematically with increasing similarity threshold δ, as shown in the inset of Fig. S1B, because looser matching criteria classify more generated structures as non-novel. Structural diversity was then quantified by evaluating uniqueness, coverage recall, and coverage precision as functions of δ. As shown in Fig. S1C, uniqueness decreases monotonically with increasing δ, whereas both coverage recall and coverage precision increase, revealing a clear trade-off between maintaining structural distinctiveness and achieving broader coverage of the target structural space.

To demonstrate the capabilities of ApolloX in structure search for amorphous systems, we initialized a PSO-based structural evolution with 100 Cond-CDVAE-generated structures as the initial population and evolved them over 15 generations. The evolution of the lowest-energy structure across generations is shown in Supplementary Fig.S1D, with the thermodynamically most favorable configuration shown in the inset. The lowest-energy amorphous $Fe_{12}Co_{12}Ni_{12}Mo_{12}B_{12}O_{60}$ structure, with an energy of -1045.39 eV, emerged by the third generation, highlighting the efficiency of the PSO algorithm in optimizing PDM-constrained energy landscapes.

To systematically elucidate the mapping between chemical short-range order (CSRO) and the potential energy landscape, we generated a statistical ensemble of 2,400 structures. Following geometric optimization, the PDM of the thermodynamically most stable configuration (lowest energy) was extracted as the reference ground-state motif. We then stratified the ensemble into four distinct groups based on the magnitude of their PDM deviation from this reference, defined as the accumulated absolute difference of matrix elements.

As illustrated in Supplementary Fig.S1E, we observe a rigorous correlation between CSRO fidelity and energetic stability: structures with PDMs closely resembling the ground state (Group 1) are confined to deep, low-energy basins, whereas those with larger PDM deviations (Groups 2–4) exhibit a systematic shift toward higher-energy, less stable regions. This monotonic broadening and shifting of the energy distribution confirm that the PDM descriptor successfully encodes essential energetic information of the amorphous network, thereby validating its rationality as a structural constraint for targeting thermodynamically stable phases in our generative model.

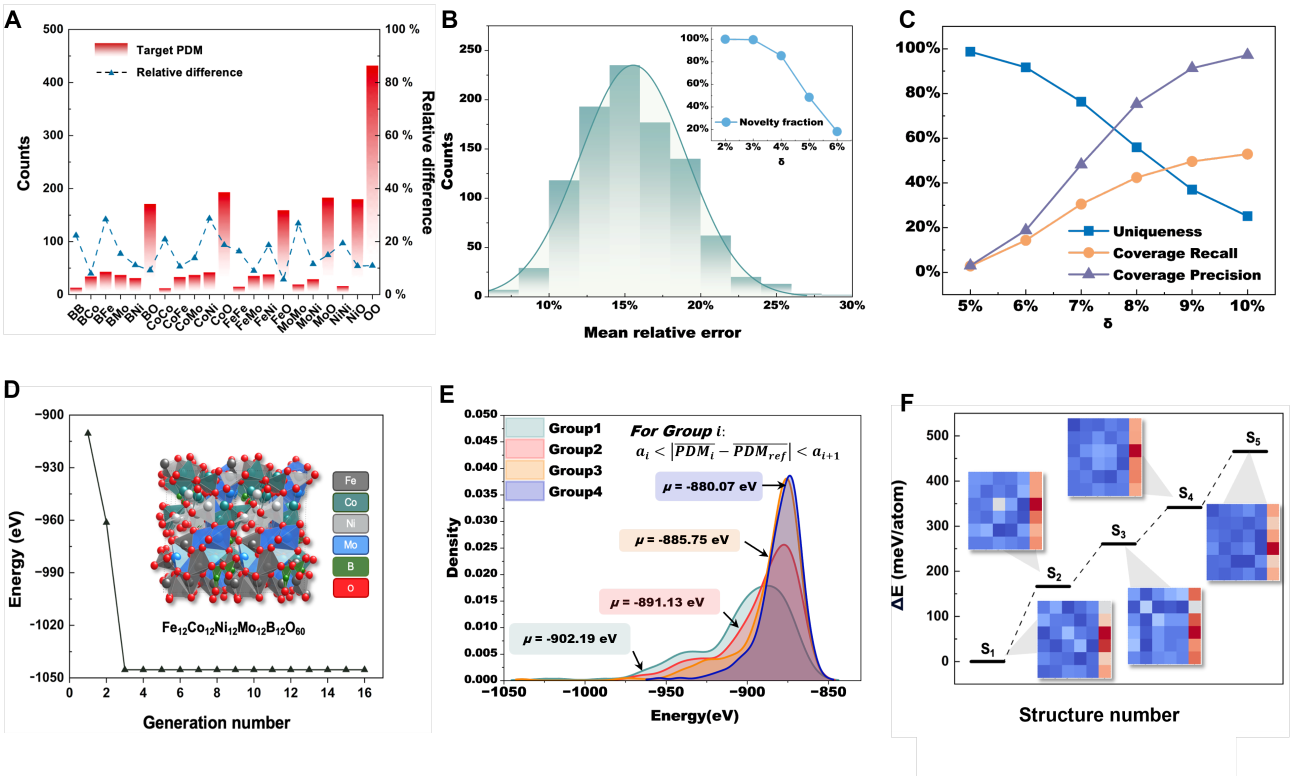

FIG. S1: **Model prediction of structural energy distribution, reconstruction accuracy, and diversity analysis.** (A) Target pair-density matrix (PDM) and the relative deviation of generated structures, demonstrating the model's ability to capture short-range ordering with high fidelity. (B) Histogram of the mean relative PDM errors for 1,000 generated structures. Inset: novelty fraction as a function of the similarity threshold δ, obtained by comparing generated structures with the 80,000-structure training set.(C)Uniqueness, coverage recall, and coverage precision plotted as functions of δ. (D) Particle-swarm optimisation (PSO) energy trajectory, showing the evolution of structure energy with generation number and a representative thermodynamically stable structure. (E) Energy distributions of structures grouped by increasing PDM deviation from the lowest-energy configuration (Group 1: smallest deviation; Group 4: largest deviation), highlighting the correlation between PDM fidelity and thermodynamic stability. (F) Lowest-energy structures obtained with ApolloX; the insets show their corresponding PDMs, exhibiting characteristic short-range-ordering motifs.

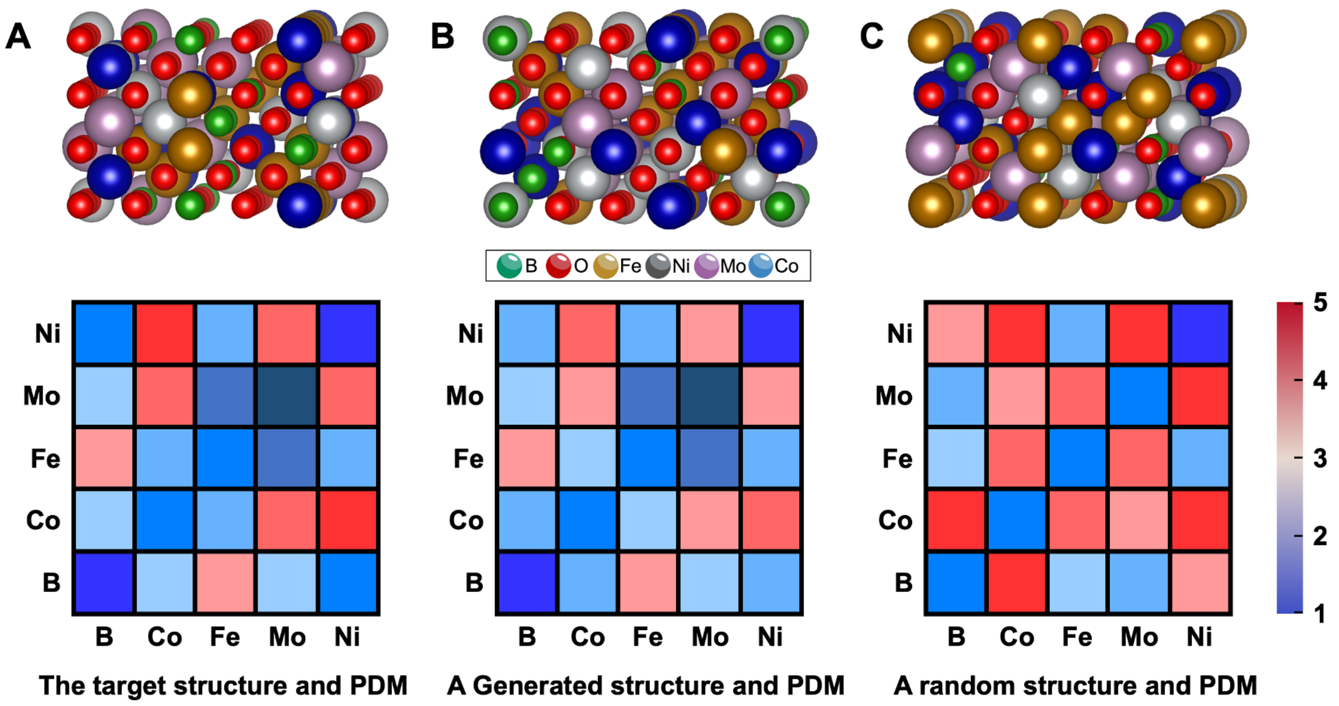

FIG. S2: **Comparison of atomic structures and their corresponding PDMs.** (**A**) The target structure and its PDM. (**B**) A generated structure and its PDM. (**C**) A random structure and its PDM. Each heatmap shows the PDM between element pairs (rows *vs.* columns), with color indicating the distance value, according to the color bar on the right.

TABLE S2: **Hyperparameters of Cond-CDVAE model used in this work.** Each element type is embedded by a vector of length 50. $\mathrm{MLP}_{\mathrm{zc}}$ is a multi-layer perceptron for concatenated latent vector and condition embedding vector. DimeNet++ and GemNet-dQ are used as $\mathrm{PGNN}_{\mathrm{Enc}}$ and $\mathrm{PGNN}_{\mathrm{Dec}}$, respectively.

Model	**Value**
Element type embedding	50
vectorized PDM dimension	197
$\mathrm{MLP}_{\mathrm{zc}}$ number of layers	3
$\mathrm{MLP}_{\mathrm{zc}}$ number of hidden channels	64
$\mathrm{MLP}_{\mathrm{L}}$ number of layers	1
$\mathrm{MLP}_{\mathrm{L}}$ number of hidden channels	256
$\mathrm{PGNN}_{\mathrm{Enc}}$ number of blocks	4
$\mathrm{PGNN}_{\mathrm{Enc}}$ number of hidden channels	128
$\mathrm{PGNN}_{\mathrm{Enc}}$ interaction embedding size	128
$\mathrm{PGNN}_{\mathrm{Dec}}$ number of blocks	4
$\mathrm{PGNN}_{\mathrm{Dec}}$ number ofhidden channels	128
Loss weight $\lambda_{\mathbf{L}}$	10
Loss weight $\lambda_{\mathbf{X}}$	10
Loss weight β	0.01
Optimizer	**Value**
Optimizer type	Adam
Learning rate	1e-4
Learning rate scheduler	ReduceLROnPlateau
Scheduler patience (epoch)	30
Scheduler factor (epoch)	0.6
Minimal learning rate	1e-5
Data	**Value**
Batch size	128

C. Comparative Energy Evaluation of BCC, FCC, and HCP Structures

We conducted energy distribution calculations on 1,500 structures for each of the BCC, FCC, and HCP configurations to ensure a comprehensive comparison. The energy distributions of these configurations are shown in Fig. S4. The results clearly demonstrate that the BCC lattice consistently outperforms FCC and HCP in terms of stability. Specifically, the average energy of the BCC system (-7.50 eV/atom) is lower than that of FCC (-7.46 eV/atom) and slightly lower than HCP (-7.34 eV/atom). The minimum energy structure in the BCC system also exhibits the lowest energy (-9.05 eV/atom) among the three lattices, indicating its superior potential to form highly stable configurations. These findings strongly support the rationality of our choice to use the BCC lattice.

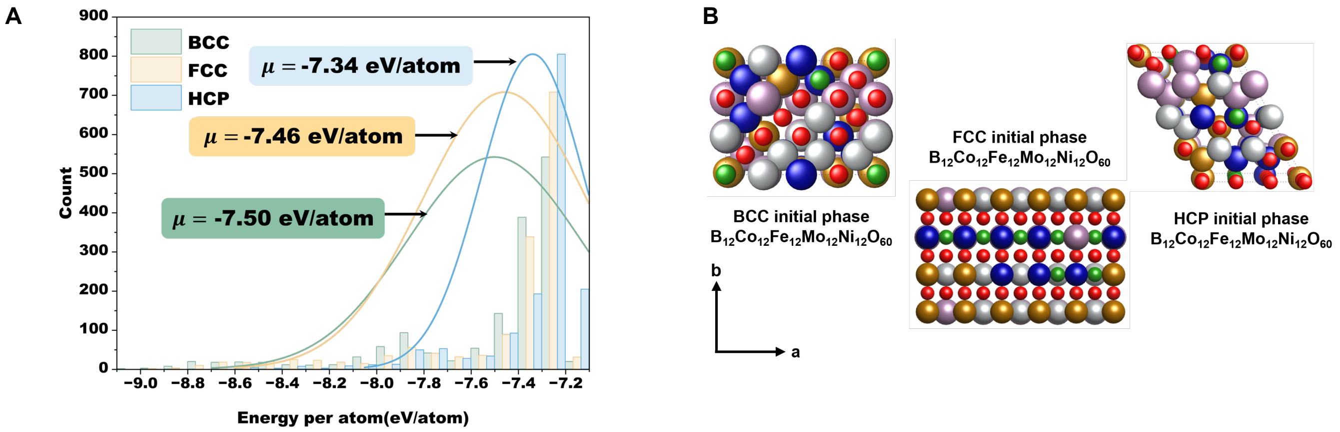

FIG. S3: **Evaluation of structural energy landscapes for different prototype configurations.** Energy distributions of 1500 generated structures initialized from three distinct crystal prototypes: body-centered cubic (BCC), face-centered cubic (FCC), and hexagonal close-packed (HCP). The BCC-initialized structures exhibit a broader distribution and lower average energy, suggesting better thermodynamic stability.

D. Hierarchical clustering dendrogram for the five lowest-energy structures.

We employ the Frobenius distance, d_F, to quantify the difference in chemical short-range order (CSRO) between structure ensembles. For two matrices $\mathbf{A}$ and $\mathbf{B}$ the Frobenius distance is defined as:

$$d_F(\mathbf{A},\mathbf{B}) = \left\|\mathbf{A}-\mathbf{B}\right\|_F = \sqrt{\sum_{i=1}^{m}\sum_{j=1}^{n}\left(A_{ij}-B_{ij}\right)^2}\,. \tag{S1}$$

In Eq. (1), $\mathbf{A}$ and $\mathbf{B}$ are real matrices of identical size $m \times n$ that contain the pair-density matrix statistics of two structure ensembles; their elements A_{ij} and B_{ij} give the coordination count (or probability) between central species i and neighbour species j. Indices $i = 1, \ldots, m$ enumerate the central atoms (or structure samples), while $j = 1, \ldots, n$ enumerate the neighbouring atom types (or feature dimensions); thus m and n define the dimensionality of the statistics. The symbol $\|\cdot\|_F$ denotes the Frobenius norm, $\|\mathbf{X}\|_F = \sqrt{\sum_{i=1}^{m}\sum_{j=1}^{n} X_{ij}^2}$. Consequently, $d_F(\mathbf{A},\mathbf{B})$ is the Frobenius distance between the two matrices, providing a quantitative measure of the overall deviation in chemical short-range order (CSRO); smaller values indicate higher similarity between the two ensembles.

First, we calculate the Frobenius distance between the PDM of the five lowest-energy structures and the mean values of PDM in different ranges, representing the differences of CSRO between the most stable structures and those within the respective ranges. For the five Apollox energy minima, we obtained $d_F \approx 100.89 \pm 20.75$; whereas structures with $E < -920\,\mathrm{eV}$ yielded $d_F \approx 290.35 \pm 68.16$. In contrast, the random pool gave $d_F \approx 385.40 \pm 69.61$, while the top-50 % high-energy pool resulted in $d_F \approx 386.97 \pm 69.63$. As the energy of structures within the range increases, the Frobenius distance between the lowest-energy structures and the range average also rises. These results confirm that low-energy structures cluster around a distinct CSRO motif and show significant differences from high-energy structures.

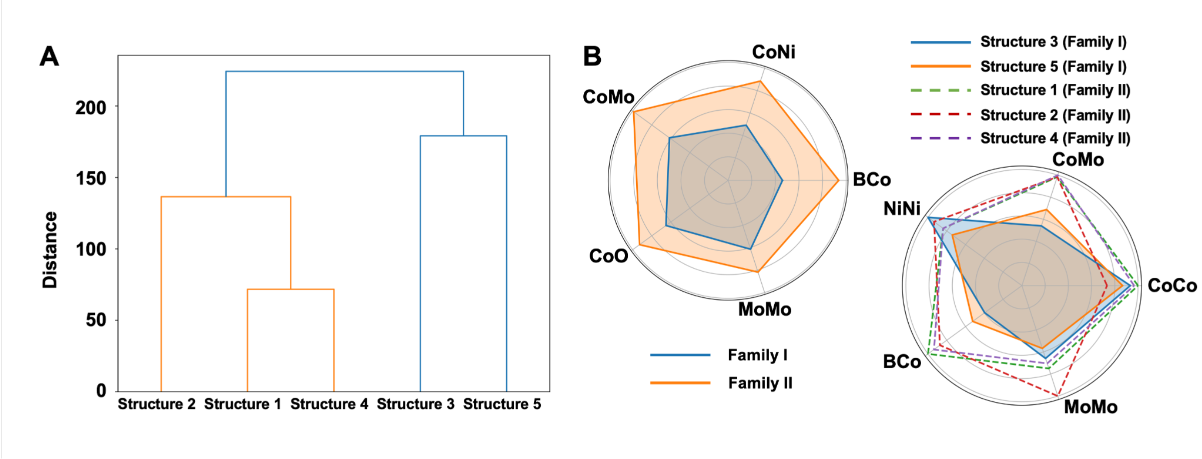

FIG. S4: **Hierarchical clustering dendrogram for the five lowest-energy structures.** The structures are divided into two families: Family I (structures 3 and 5) and Family II (structures 1, 2, and 4). Normalized PDM radar charts for key atomic pairs illustrating the intra-family similarities and inter-family differences between the five lowest-energy structures. (**A**) Radar chart of the five atomic pairs with the largest relative differences between the two families. (**B**) Radar chart of the five atomic pairs selected based on strong intra-family similarity across both families, ranked by their similarity within each family.

To further explore the differences among the five lowest-energy structures, we performed hierarchical clustering based on their Frobenius distances with each other, resulting in a dendrogram (Fig. S4A) that shows the structures are divided into two distinct families. To better illustrate the characteristics and differences between these two families, we created normalized PDM radar charts for key atomic pairs (Fig. S4B). In Fig. S4B left, the radar chart highlights the five atomic pairs with the largest relative differences between the two families. In Fig. S4B right, the radar chart displays the five atomic pairs selected based on strong intra-family similarity across both families, ranked by their similarity within each family. Notably, the atomic pairs B-Co, Co-Mo, and Mo-Mo appear in both charts. This indicates that these three atomic pairs exhibit similarity within the same family and significant differences between the two families. Therefore, it can be concluded that for Family 1 (structures 3 and 5), the coordination numbers of B-Co, Co-Mo, and Mo-Mo are relatively low, whereas for Family 2 (structures 1, 2, and 4), these coordination numbers are relatively high. The maximum differences in PDM for these three atomic pairs across the five structures reach 60.32 %, 45.90 % and 43.18 %, respectively. These differences may account for the observed differences in catalytic behavior.

E. Normalized variance of PDM

To investigate the chemical short-range order of the structure, we first computed the variance of atomic pairs in the PDM across different energy ranges. This variance reflects the uniformity and consistency of atomic pair coordination within specific energy ranges. Specifically, atomic pairs with smaller variances exhibit better coordination consistency within a given energy range. Atomic pairs that retain smaller variances in low-energy regions are likely to play a significant role in the structural stability, while atomic pairs with larger variances demonstrate greater spatial dispersion and may contribute less to structural stability.

Actually, the variance of atomic pair coordination numbers is also correlated with their mean values. To simplify the comparison of the relative consistency of atomic pair coordination numbers, we use the variance-to-mean ratio for subsequent statistical analysis. For structures across all energy ranges, the variance-to-mean ratios of different atomic pairs are shown in Fig. S5. Oxygen-oxygen pairs are excluded due to their significantly larger variance, which would affect the observation of other atom pairs.

PDM is classified into self-pair interactions, intermetallic pairs, and metal-oxygen interactions. The variance-to-mean ratio of the PDM in the energy ranges below and above −920 eV is shown in Fig. S6. It can be observed that, regardless of whether the energy is less than or greater than −920 eV, the variance of self-pair interactions is always smaller than that of intermetallic pairs, which in turn is smaller than that of metal-oxygen pairs. However, the relative ordering of these three atomic pair groups varies across different energy ranges. For the more stable structures with energies below -920 eV, it is notable that some Ni-X pairs (such as Ni-Ni, Fe-Ni, and B-Ni), as well as B-B pairs, have relatively small coordination number variances, suggesting that these atomic pairs may play a crucial role in forming stable structures and significantly impact the chemical short-range order of the structure.

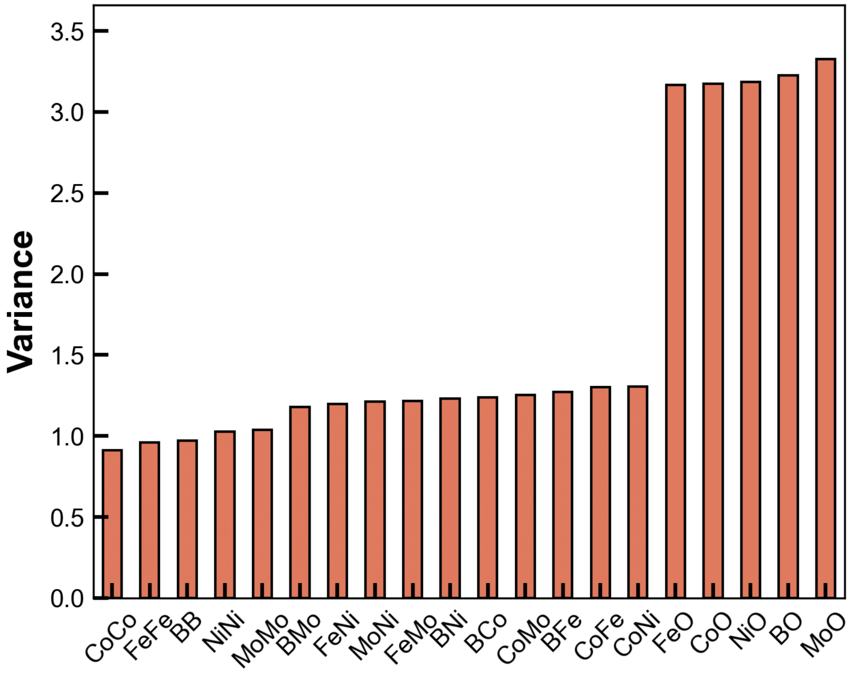

FIG. S5: **Variance-to-mean ratio of PDM across all energy ranges.**

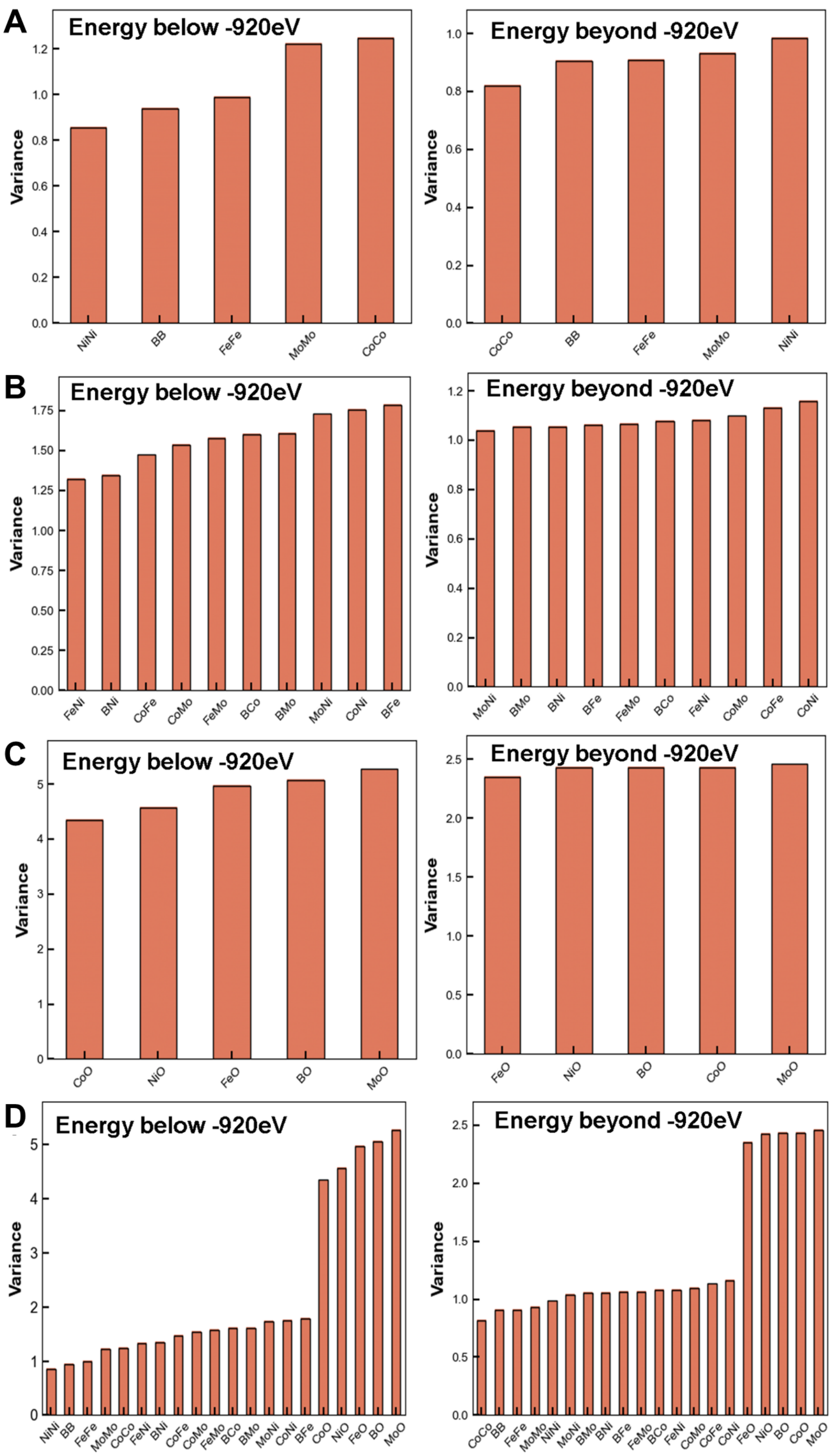

FIG. S6: **Normalized variance analysis of pair distributions.** (**A**) Variance of elemental pairs. (**B**) Variance of intermetallic pairs. (**C**) Variance of metal-oxygen pairs. (**D**) Variance of all elements in the pair distribution matrix. The variance is normalized by dividing it by the corresponding mean value.

F. Validation of DPA-2 Energy Accuracy Against DFT Calculations

To evaluate the predictive accuracy of the DPA-2 machine-learned potential, we compared its energy estimations against density functional theory (DFT) calculations across a set of representative structures. The energy discrepancies, defined as $\Delta E_{\mathrm{DFT-DPA2}}$, are summarized in Fig. S7. Overall, the majority of structures exhibit excellent agreement between DPA-2 and DFT, with absolute energy differences falling within ±5 meV/atom. This level of accuracy is comparable to typical thresholds reported for high-quality machine-learned interatomic potentials.

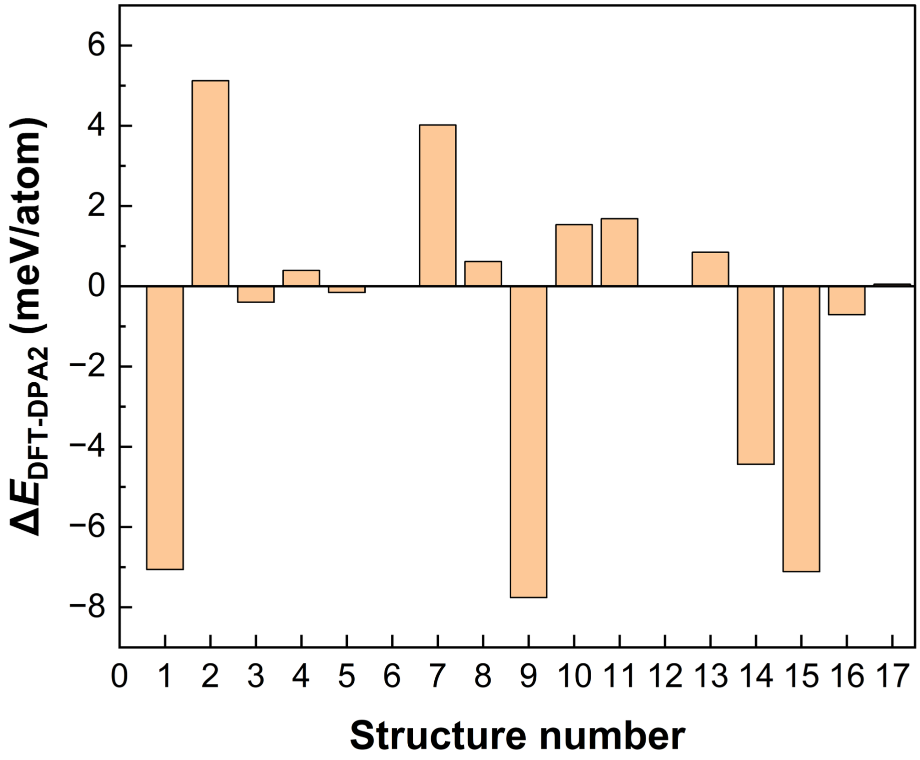

FIG. S7: **Accuracy analysis of DPA-2.** Compared the energy differences between DFT and DPA-2 for structures within different energy intervals to evaluate the accuracy of the MLP. The horizontal axis represents the number of structures, while the vertical axis shows the energy discrepancy between DFT and DPA-2 for each respective structure.

G. Diffusion rate analysis

The diffusion rate (D) can be inferred from the slope of the MSD curve, which can be calculated as:

$$\langle (r(t) - r(0))^2 \rangle = 6Dt \tag{S2}$$

As the boron content increases, the overall diffusion rate of the system decreases, as shown in Fig. S8A. This trend is also observed for metal and boron species (Fig. 3C in the main text) and oxygen components (Fig. S8B). Additionally, oxygen atoms exhibit higher diffusion rates compared to metals and boron, with boron being the most sluggish component. Consequently, boron plays a key role in determining the crystallization rate, which in turn influences the degree of amorphization.

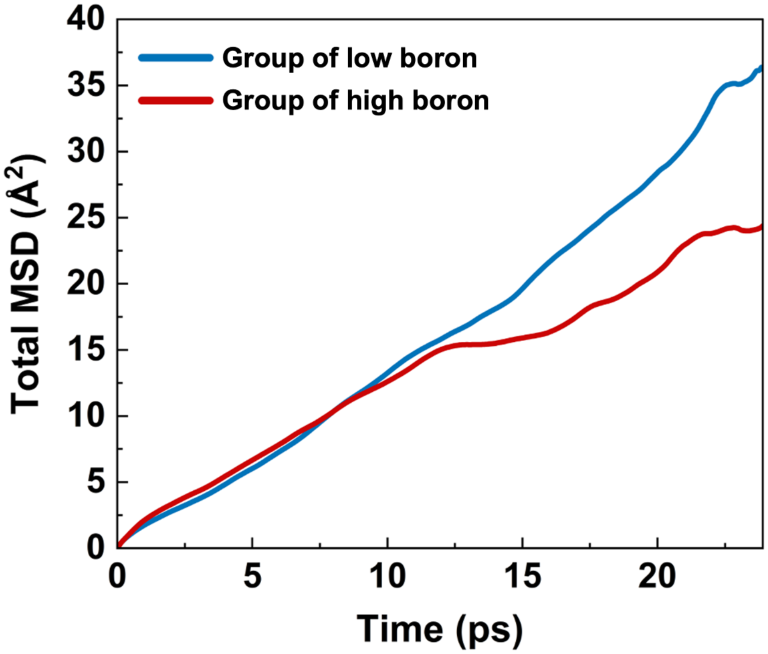

FIG. S8: **Diffusion rate analysis across groups with different boron contents. a** Diffusion coefficients for all atoms. Molecular dynamics simulations were performed under a slow heating ramp from 300 K to 2050 K over a total duration of 24 ps.

H. Characterization

Using a cryo-TEM holder working at -193 °C (tip temperature is -179 °C), we acquired aberration-corrected atomic-resolution annular dark-field scanning transmission electron microscopy (ADF-STEM) images of samples.

Direct evidence of amorphization

We have conducted synchrotron X-ray diffraction experiments as shown in Fig. S9. The resulting pair distribution functions (PDFs) and 2D diffraction patterns provide direct evidence of amorphization and further support the simulation results.

Compared with the crystalline LaB_6 standard, all three synthesized samples lack distinct Bragg reflections, confirming the absence of long-range order. Moreover, from Group-1 to Group-3, the broadening and fading of diffraction rings reflect increasing structural disorder with higher boron incorporation. The corresponding 1D intensity profiles and PDFs demonstrate the suppression of medium- and long-range correlations, consistent with amorphous behavior. These observations align with our simulations and further substantiate the claim that increasing boron content promotes amorphization.

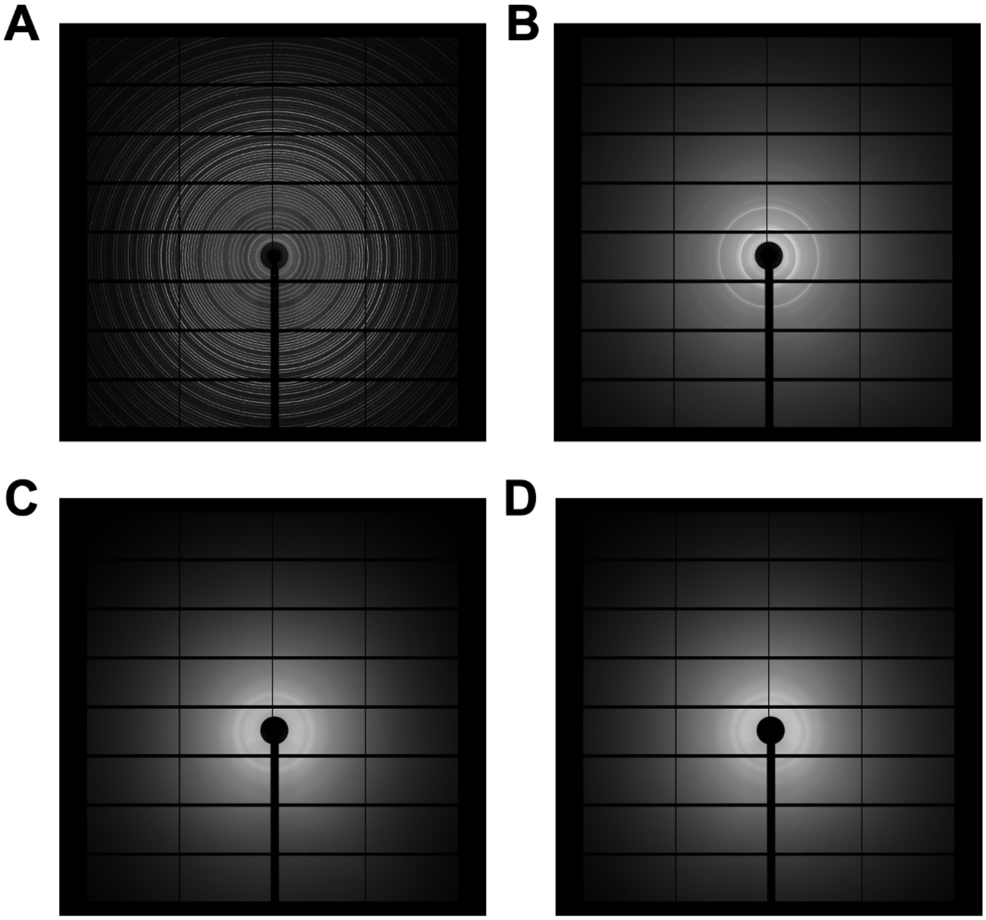

FIG. S9: **Synchrotron X-ray diffraction patterns of reference and experimental samples.** (**A**) Reference LaB_6 exhibits sharp and well-defined diffraction rings, characteristic of a crystalline standard. (**B**–**D**) Diffraction patterns of Group-1, Group-2, and Group-3 samples, respectively, showing a progressive loss of ring sharpness and increased halo-like features with higher boron content, indicating enhanced amorphization.

TABLE S3: **Elemental compositions of catalysts estimated from ICP and element analysis.** Metallic contents were determined by ICP, and O contents were detected by difference subtraction of mass conservation.

Catalyst	Fe (mol %)	Co (mol %)	Ni (mol %)	Mo (mol %)	B (mol %)	O (mol %)
Group-1	8.74	8.23	8.26	6.93	5.87	61.98
Group-2	9.02	8.65	8.62	6.45	8.47	58.79
Group-3	10.36	10.03	9.94	7.23	11.68	50.76

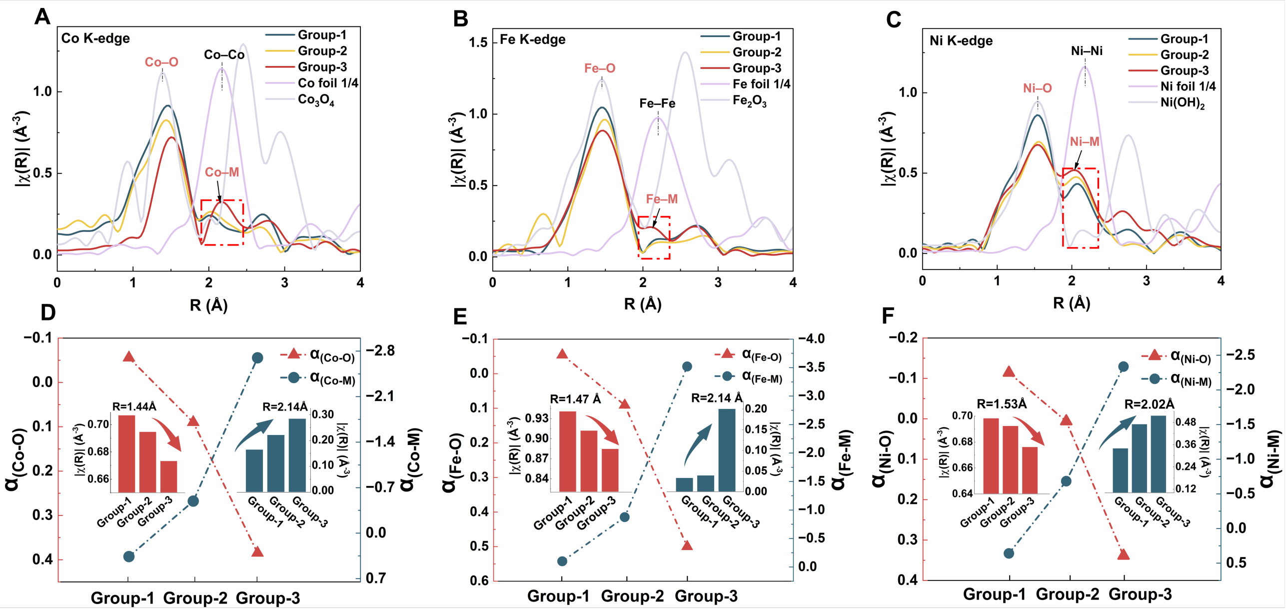

FIG. S10: **Structural characterization and interaction analysis.** (**A** to **C**) Fourier-transformed EXAFS spectra of Fe, Co, and Ni K-edges in R-space. (**D** to **F**) α_{ij} values for M–O and M–M (M = Co, Fe, Ni) interactions derived from predicted structures of FeCoNiMoBO$_x$ in three groups, compared with the magnitude of $|\chi|(R)$ from EXAFS. Positive α_{ij} values indicate dispersion, while negative values correspond to aggregation.

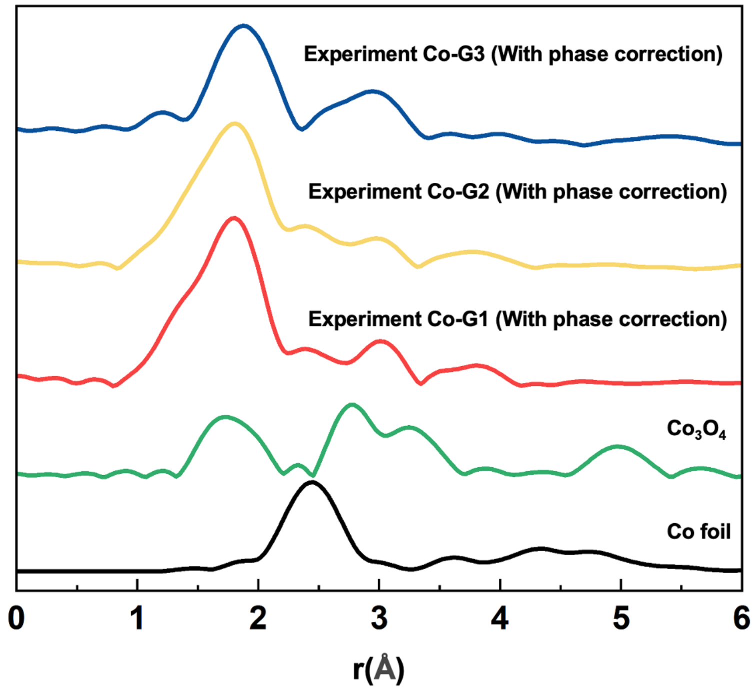

FIG. S11: **Fourier-transformed EXAFS spectra of Co-based samples.** Experimental Co-G1, Co-G2, and Co-G3 spectra after phase correction are compared with reference spectra of Co foil and Co_3O_4 in R-space. Phase correction aligns the experimental peaks with the actual interatomic distances, enabling accurate structural comparison of the local coordination environment around Co atoms.

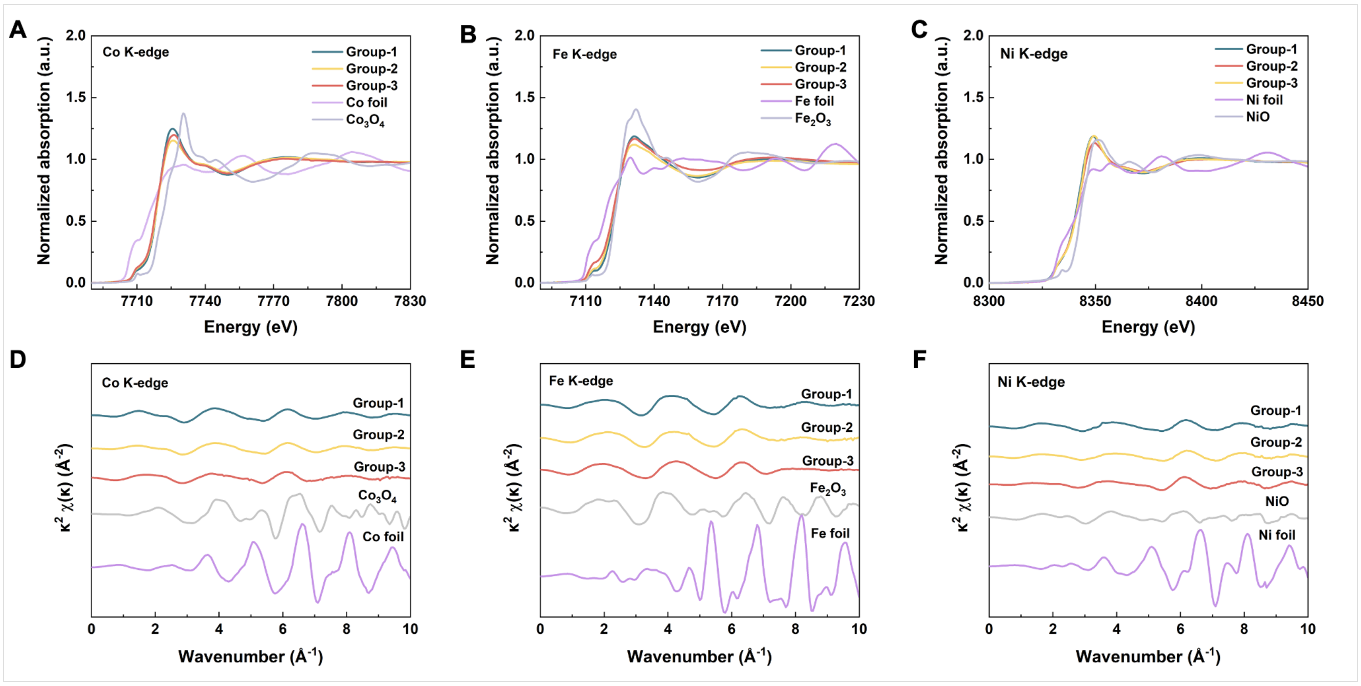

FIG. S12: **XAS and EXAFS analysis at the Co, Fe, and Ni *K*-edges.** (**A**–**C**) Normalized XANES spectra at the Co, Fe, and Ni *K*-edges for Group-1, Group-2, and Group-3, compared with corresponding metal foils and oxides. The absence of distinct post-edge features associated with Co–Co, Fe–Fe, and Ni–Ni coordination confirms the lack of long-range metal ordering. (**D**–**F**) Corresponding *k*-space EXAFS spectra ($k^2\chi(k)$). The dampened and broadened EXAFS signals in the experimental groups indicate increased structural disorder and amorphization relative to the crystalline standards.

TABLE S4: **Co K-edge EXAFS fitting parameters for FeCoNiMoBO$_x$ samples with varying boron contents.** Fitting results are shown for Group-1, Group-2, and Group-3, where M = Fe/Co/Ni/Mo. The coordination number (N), Debye–Waller factor (σ^2), and bond distance (R) are extracted from two-shell fits covering 1.00–2.40 Å (Co–O) and 2.50–3.85 Å (Co–M) ranges. With increasing boron content, $N_{\mathrm{Co-O}}$ decreases while $N_{\mathrm{Co-M}}$ increases, indicating a structural transition from oxygen-bridged Co–O–Co linkages toward direct metal–metal interactions. All σ^2 values remain physically reasonable, and low R-factors (0.01276–0.31000) confirm good fitting quality.

Group	**Name**	**N**	$\boldsymbol{\sigma^2}$	**R (Å)**	**r-factor (%)**
Group-1	O	1.000	0.01197	1.82359	0.01276
	O	2.914	0.01284	1.89610	
	O	2.383	0.00323	2.03618	
	M	0.478	0.00426	2.52069	
Group-2	O	2.000	0.01122	1.88906	0.02232
	O	1.500	0.00299	2.04353	
	O	1.110	0.00292	2.32660	
	M	0.621	0.00784	2.57409	
Group-3	O	1.641	0.00648	1.89911	0.31000
	O	1.354	0.00298	2.00070	
	O	0.600	0.02000	2.13367	
	M	1.000	0.00619	2.43548	

I. Catalytic performance of Group1-3

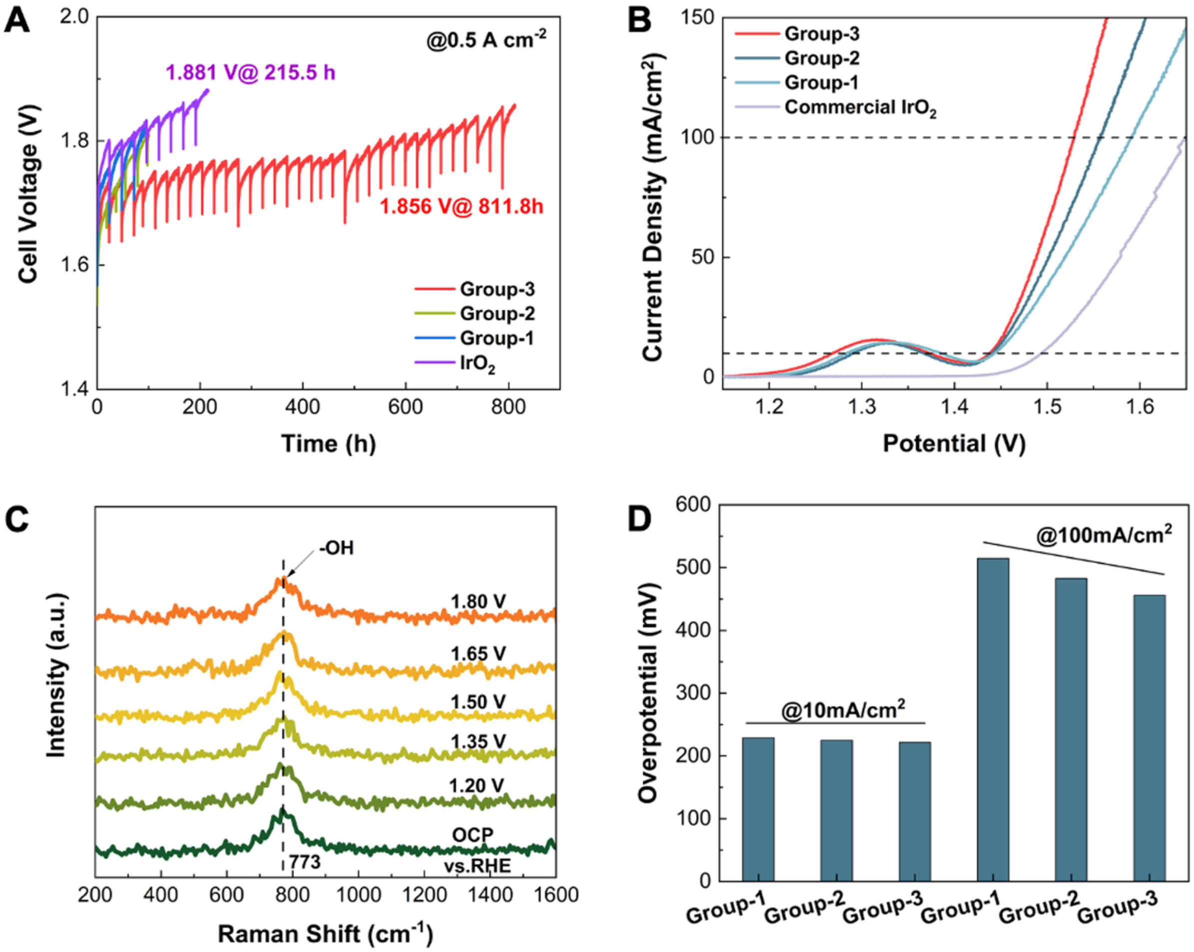

FIG. S13: **Catalytic stability.** (**A**) Stability test at 0.5 A/cm^2 using an anion exchange membrane (AEM) device for different groups, compared with IrO_2. (**B**) In-situ Raman spectra of $FeCoNiMoBO_3$ (Group-3). In situ Raman spectroscopy shows no detectable metal oxide vibrations (e.g., E_{2g}, A_{1g}) and a dominant $-OH$ peak at 773 cm^{-1} persisting across applied potentials, indicating structural stability. (**C**) OER overpotentials across different groups at varying current densities. (**D**) Linear sweep voltammetry curves of Group-1, -2, and -3, compared with commercial IrO2.

J. Structural characterization of the twelve-component FeCoNiCuMnZnMoWAlSnBO$_x$ sample

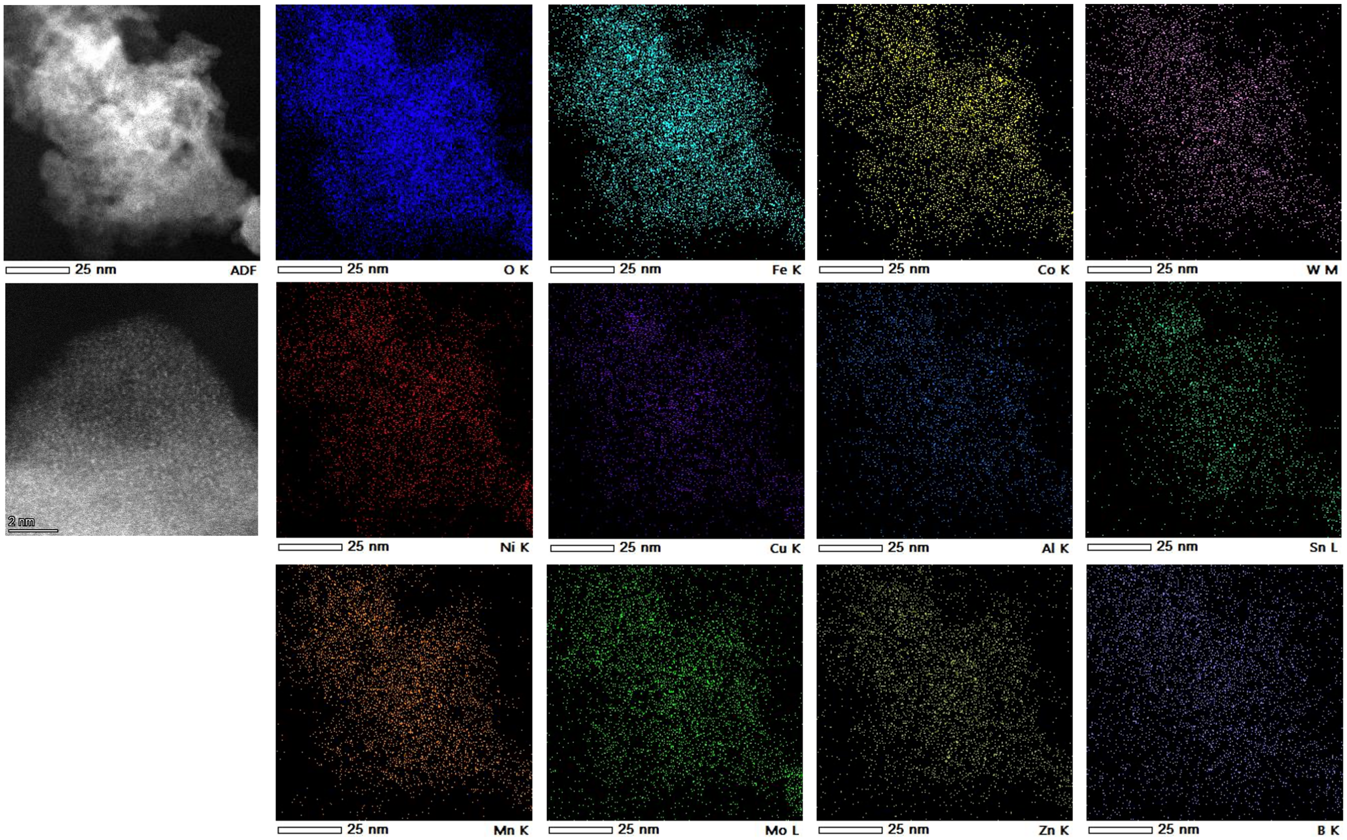

FIG. S14: **Characterization of the twelve-component FeCoNiCuMnZnMoWAlSnBO$_x$ sample.** ADF-STEM and high-magnification TEM images of the as-synthesized particle, together with STEM–EDS elemental maps of O, Fe, Co, W, Ni, Cu, Al, Sn, Mn, Mo, Zn, and B. The similar spatial distributions of all elements indicate a chemically homogeneous amorphous multicomponent boroxide without obvious phase segregation or element-rich domains. Scale bars: 25 nm (ADF-STEM and EDS maps) and 2 nm (TEM image).